Evolutions of the Micro- and Macrostructure and Tensile Property of Cu-15Ni-8Sn Alloy During Electromagnetic Stirring-Assisted Horizontal Continuous Casting

ZHE SHEN, BANGFEI ZHOU, JIE ZHONG, YUNBO ZHONG, TIANXIANG ZHENG, LICHENG DONG, YONG ZHAI, WEILI REN, ZUOSHENG LEI, and ZHONGMING REN

The present study investigates the evolution of the micro- and macrostructure and tensile property of the Cu-15Ni-8Sn (weight percent) alloy prepared by horizontal continuous casting and electromagnetic stirring (EMS). The results show that the application of EMS is beneficial for grain refinement and for microstructure transformation from the dendrite to the rosette structure and that it leads to a significant improvement in the tensile property. The forced flow induced by EMS homogenizes the temperature field ahead of the solid-liquid interface, disturbing the heat flow direction and resulting in the columnar to equiaxed transition. The grain refinement under different electromagnetic stirring frequencies is mainly derived from the homogenization of the temperature and the remelting of dendritic arms. In addition, the evolution of the tensile property with and without EMS is discussed from the perspective of fracture mode and fine-grain strengthening.

I. INTRODUCTION

THE Cu-Ni-Sn alloys are expected to replace the Cu-Be alloys and have been widely used for electrical switchgear, springs, and connectors due to their high corrosion resistance, high thermal conductivity, and excellent electric conductivity after aging heat treatment.[1–3] Continuous casting is an excellent method for producing aluminum alloys[4,5] and copper alloys[6,7] with high manufacturing efficiency. However, the traditional continuous casting method also presents some difficult technical problems such as highly columnar macrostructure,[8] severe segregation,[9] and shrinkage porosity.[10] These problems will result in weak hot working performance during the forging or rolling process, thereby yielding poor mechanical properties. Grain refinement is an effective way to improve the

deformability and tensile strength of the alloys. The adjustments of casting parameters, such as the cooling rate and pouring temperature, the addition of grain refinement agents, and mechanical stirring, are common methods used to achieve grain refinement. However, these methods either have limited effects on grain refinement or give rise to impurities.

Electromagnetic stirring (EMS) has been used to modify the columnar to equiaxed transition (CET)[11,12] and then to refine the grain size.[13,14] Many studies on the CET and refinement mechanism have been reported. Willers et al.[15] found the CET in the unidirectional solidification of Pb-Sn alloys under a rotating magnetic field and suggested that the forced convection leads to a reduction in the temperature gradient ahead of the solidification front and then induces the remelting of the dendrites at certain locations because of the remarkable temperature fluctuations in the mushy zone. Campanella et al.[16] found that the efficiency of EMS depends strongly on the penetration of the liquid in the mushy zone and developed a dendrite fragmentation criterion to explain the grain refinement. Moreover, the forced convection induced by EMS can also influence the dendritic growth. Dendritic morphology undergoes a significant transformation from the dendrite to rosette structure due to its rotation under streamlined flow or a periodic change in the fluid flow direction around the growing solid.[17] In addition, the improvement in the

ZHE SHEN, BANGFEI ZHOU, JIE ZHONG, YUNBO ZHONG, TIANXIANG ZHENG, LICHENG DONG, YONG ZHAI, WEILI REN, ZUOSHENG LEI, and ZHONGMING REN are with the State Key Laboratory of Advanced Special Steel & Shanghai Key Laboratory of Advanced Ferrometallurgy & School of Materials Science and Engineering, Shanghai University, Shanghai 200072, China. Contact emails: yunboz@staff.shu.edu.cn, ztx@shu.edu.cn
Manuscript submitted April 5, 2019.
Article published online August 26, 2019.

strength can be obtained by the fine-grain strengthening according to the Hall–Petch relationship.[18,19] However, the tensile strength is also affected by the dendrite. Kato[20] showed that the tensile property in the growth direction is controlled by dendritic solute segregation that depends on the primary arm spacing or dendritic morphology, while the tensile strength perpendicular to the growth direction is largely influenced by casting defects such as cavities. For casting alloys, second phase and casting defects will exist in the interdendritic regions, possibly giving rise to a significant impact on the tensile strength.

In this study, EMS was applied to obtain a fine, uniform equiaxed grain structure with a high tensile strength during the horizontal continuous casting of the Cu-15Ni-8Sn alloy. The effects of the electromagnetic stirring frequency (EMSF) on the micro- and macrostructure, tensile strength, and the relationship between the grain size, microstructure, and tensile strength were investigated. Furthermore, the refinement mechanism was analyzed from the perspective of the homogenization of temperature and the remelting of the dendritic arms. The evolution of tensile strength was discussed from the perspective of the fracture mode and fine-grain strengthening.

II. EXPERIMENTAL PROCEDURES

4N (99.99 pct purity) electrolytic copper pieces were placed into an induction furnace and heated to 1473 K. After the electrolytic copper was melted, the 4N (99.99 pct purity) electrolytic nickel and 4N (99.99 pct purity) tin pieces were added into the melt quickly according to the target content ratio. Fish-scale carbon was used to cover the melt surface and prevent oxidation. The alloy melt was magnetically stirred for half an hour to maintain the uniformity of the alloy and then horizontally continuously cast into a long rod-shaped ingot with a diameter of 32 mm. Figure 1(a) shows the schematic diagram of the experimental apparatus. The withdrawal velocity was 100 mm/min. An EMS coil group was set outside the crucible to induce the stirring flow ahead of the solid-liquid interface during the horizontal continuous casting. The excitation current of EMS was 120 A in all of the experiments conducted in this work. The excitation current frequencies, that is, the EMSFs, were set to 6, 12, 30, and 50 Hz.

The sample with a length of 45 mm cut from the horizontal continuous casting ingot obtained under different EMSFs was sectioned parallel and perpendicular to the withdrawal direction (Figure 1(b)), and then mechanically polished and etched in a solution of concentrated nitric acid to expose the micro- and macrostructure. The micro- and macrostructure of the sample were examined by optical microscopy (Keyence VW-9000). The average diameter of a grain was measured using the centroidal method; i.e., the mean length of the grain was obtained at 2 deg intervals when passing through the grain's centroid.[21] This operation was automatically completed using the Image Pro software package. In each of the sample microstructures, four different regions were used and then the size of each grain was measured in order to obtain a reliable value for the average grain diameter. A scanning electron microscope (SEM, Tescan VEGA 3 Easy Probe) equipped with an energy dispersive spectrometer (EDS) was used to observe the morphology and distribution of the Sn-rich phase. The horizontal continuous casting ingot was cut and machined into a standard cylindrical shape (12 mm in diameter and 150 mm in length) for tensile tests. Tensile tests were
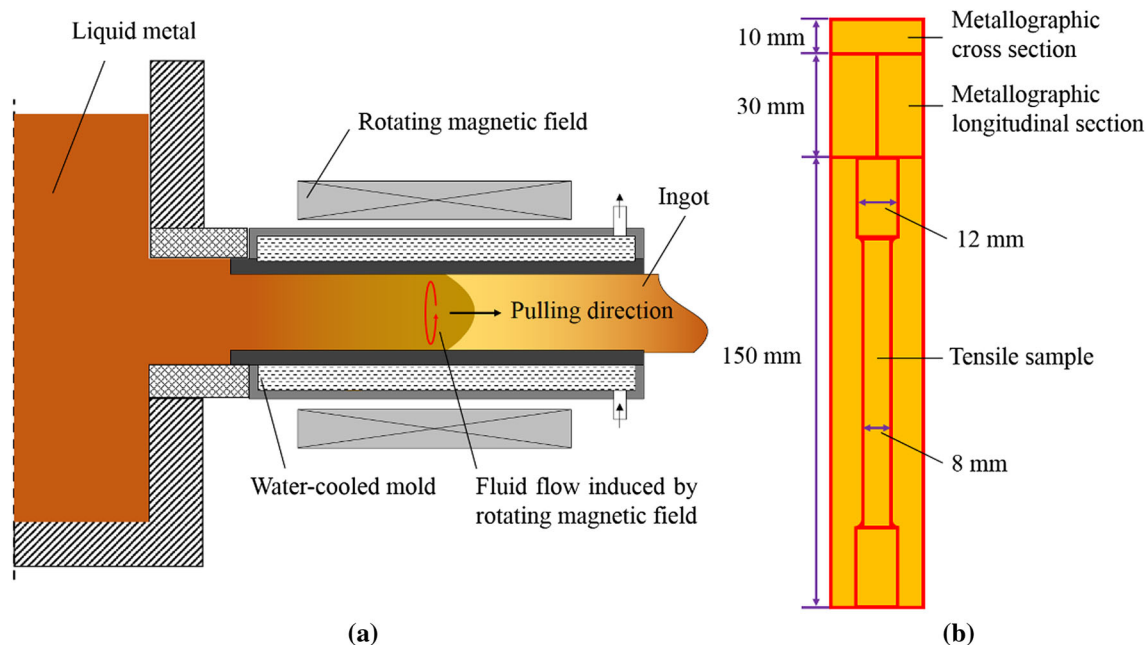

Fig. 1—Schematic diagram of the experimental apparatus and sample cutting: (a) experimental apparatus and (b) sample cutting.

performed using a CMT5105 electronic universal-testing machine at room temperature (294 K). To reduce the experimental error, the standard tensile samples were tested three times at each set of conditions.

III. EXPERIMENTAL RESULTS

A. *Metallographic Structure*

The macrostructures on the cross section and longitudinal section of the ingots with and without EMS are shown in Figure 2. Figures 2(a1) and (a2) show the macrostructure of the sample without EMS, and it is observed that the macrostructure is composed of a surface refined equiaxed grain region and a central coarse columnar grain region. This is consistent with the typical macrostructure of the as-cast ingot, indicating that due to the presence of an external water-cooled mold, there is a certain temperature gradient at the solidification front during horizontal continuous casting that gives rise to the formation of columnar grains. Moreover, the columnar grain length in the radial direction is larger than that in the withdrawal direction. This indicates that during horizontal continuous casting, the heat is mainly released along the radial direction rather than along the withdrawal direction. When a 6 Hz EMS is applied, the central coarse columnar grains are replaced by the refined equiaxed grains, as shown in Figures 2(b1) and (b2). This indicates that the original radial temperature gradient disappears under the action of EMS and the solidification of the sample is a nearly isothermal solidification. In addition, the equiaxed grains become clearly more refined with the increase in the EMSF, as shown in Figures 2(c1) through (e2). The average grain size at the different EMSFs was determined and the results are shown in Figure 3. The results show that the grains are coarser and that the average grain size is approximately 2.3 mm when EMS is not applied. The average grain size rapidly decreases to approximately 820 μm under a 6 Hz EMS. The average

grain size further decreases with the increase in the EMSF. As the EMSF increases to 50 Hz, the average grain size decreases to approximately 430 μm.

Figure 4 shows the microstructures of the different regions on the cross section and longitudinal section of the sample with and without EMS. It can be easily found that the dendrites are well developed and have distinctive growth directions (marked by the yellow arrows) from the surface to the center when EMS is not applied, as shown in Figures 4(a1) through (a3) and (b1) through (b3). This indicates that there is a certain heat flow direction from the center to the surface during solidification, which is consistent with the macrostructure observations. When EMS is applied at the frequency of 6 Hz, clear changes are observed. Most of the dendrites become less developed and the dendrite growth direction becomes more random, as shown in Figures 4(c2), (c3) and (d1) through (d3). This indicates that the temperature gradient in the center region of the sample disappears under a 6 Hz EMS. However, the dendrites at the surface region are still well developed
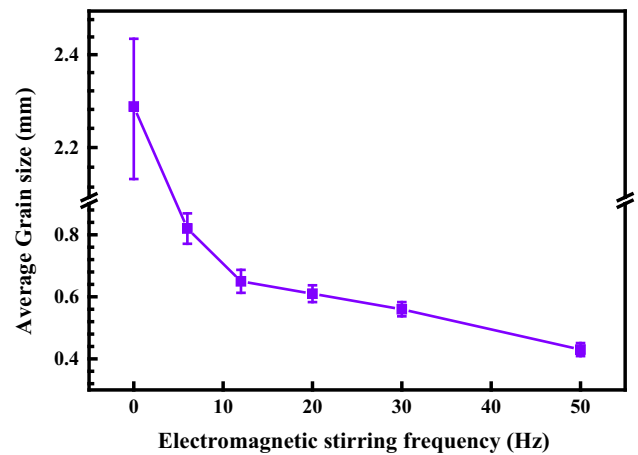

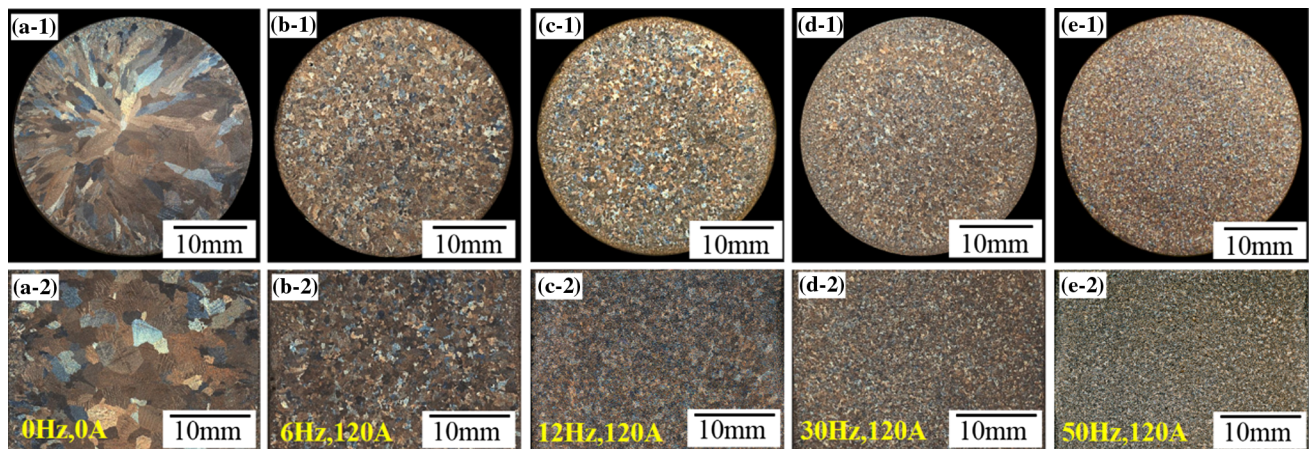Fig. 3—Relationship between the average grain size and EMSF.

Fig. 2—Macrostructures of the cross section and longitudinal section with and without EMS: (*a*1) and (*a*2) 0 Hz, 0 A; (*b*1) and (*b*2) 6 Hz, 120 A; (*c*1) and (*c*2) 12 Hz, 120 A; (*d*1) and (*d*2) 30 Hz, 120 A; and (*e*1) and (*e*2) 50 Hz, 120 A.
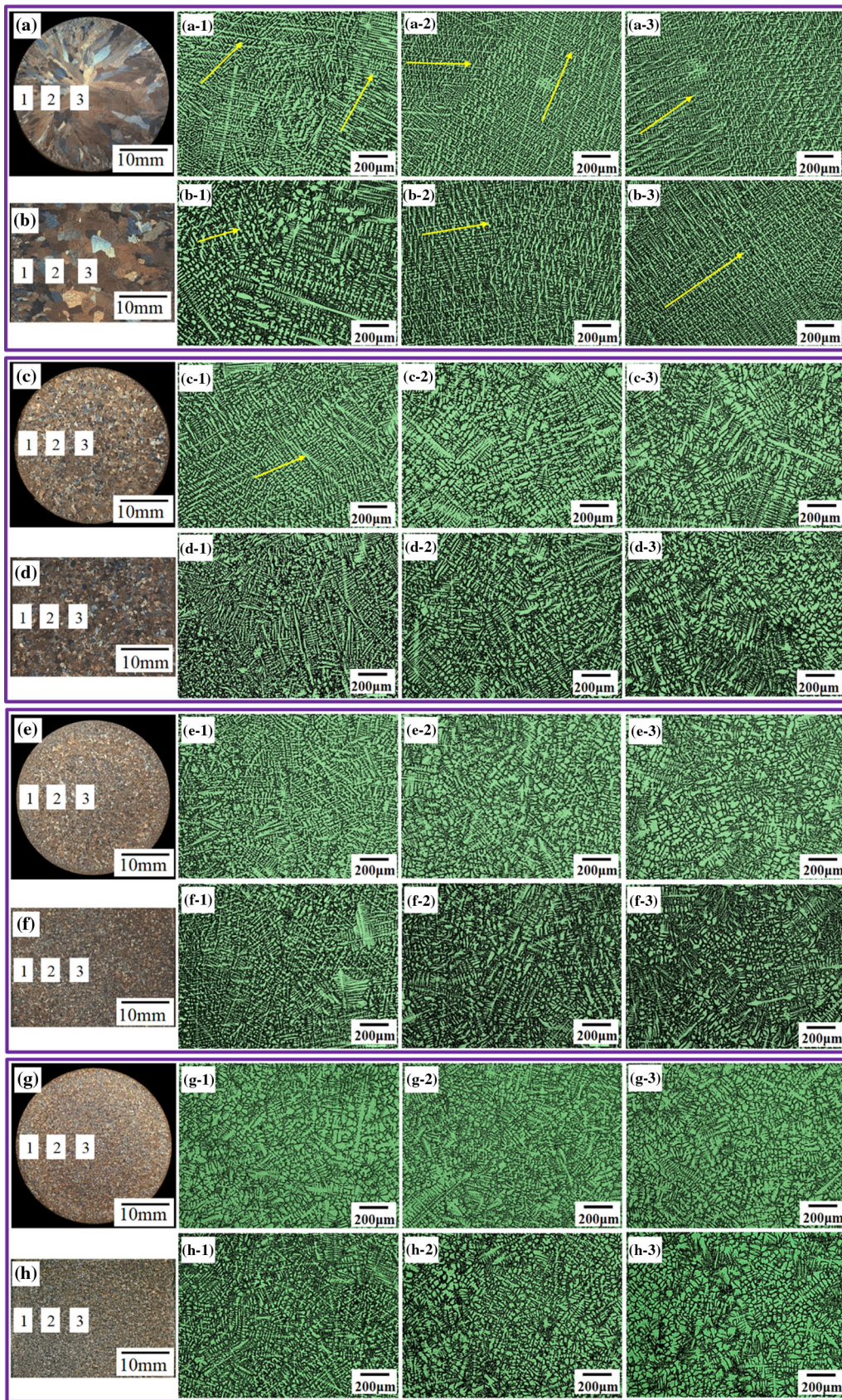
Fig. 4—Microstructures of the different regions on the cross section and longitudinal section of the sample with and without EMS: (*a*) through (*a*3) and (*b*) through (*b*3) 0 Hz, 0 A; (*c*) through (*c*3) and (*d*) through (*d*3) 6 Hz, 120 A; (*e*) through (*e*3) and (*f*) through (*f*3) 30 Hz, 120 A; (*g*) through (*g*3) and (*h*) through (*h*3) 50 Hz, 120 A.

and have a clear growth direction (Figure 4(c1)). This indicates that a temperature gradient is still present near the surface region of the sample, inducing the orientation growth of the dendrite. When EMSF increases to 30 Hz, the well-developed dendrites are hardly observed on the cross section or longitudinal section of the sample even at the surface region. The microstructures at the surface and center regions present undeveloped or equiaxed dendrites (Figures 4(e1), (e2), (f1) and (f2)). A rosette structure appears at the central regions of the cross section and the longitudinal section, as shown in Figures 4(e3), (f3). When EMSF increases further to 50 Hz, the rosette structure occupies both the cross and longitudinal sections (Figures 4(g1) through (h3)).

B. Tensile Property

When EMS is applied, the solidification structure of the sample is composed of equiaxed grains and the equiaxed grain size decreases with the increase in the EMSF. Figure 5 shows the relationship between the measured tensile strength and uniform elongation as a function of the EMSF value. The tensile strength is approximately 450 MPa under a 6 Hz EMS, as shown in Figure 5(a). The tensile strength increases with the EMSF increasing from 6 to 50 Hz, which is consistent with the change in the grain size. This indicates that the increase in the tensile strength is related to the refinement of the equiaxed grains. The uniform elongation also decreases with the increase in the tensile strength when EMSF increases from 12 to 50 Hz, as shown in Figure 5(b). The tensile strength of the sample without EMS is approximately 480 MPa, which is close to that with a 12 Hz EMS and lower than that with a 30 Hz EMS. It is noted that the solidified structure without EMS (mainly coarse columnar grains) is different from that with EMS (mainly equiaxed grains). The difference in the tensile strength for the samples with and without EMS may be related to the difference in the solidified structure. Additionally, the tensile strength is also related to the tensile direction with respect to the grain texture, particularly for the columnar structures obtained without EMS. Therefore, the relevant fracture mechanism was studied further, as described in Section IV–B.

C. Distribution of the Sn-Rich Phase

The pseudo-binary phase diagram of Cu-Ni-Sn (at the isopleth of 15 wt pct Ni) constructed based on the data available in the literature is shown in Figure 6(a).[2] The Sn-rich phase will precipitate on the dendrite boundary of the α-Cu solid solution phase when the temperature gradually decreases. Backscattering electron (BSE) images of typical as-cast Cu-15Ni-8Sn alloy are presented in Figures 6(b) and (c). Two main phases can be observed: an α-Cu solid solution phase and a small fraction of an Sn-rich phase, which is consistent with the phases shown in Reference 22. Figure 6(d) shows the element distribution in these phases. The black region marked by the yellow arrow C in Figure 6(c) is the α-Cu solid solution phase. The bright white region marked by the yellow arrow A is the Sn-rich phase distributed in the interdendritic region. The region with an intermediate gray color between the α-Cu solid solution phase and the Sn-rich phase is a transition region that is marked by the yellow arrow B. The compositions of these three regions were quantified by the EDS and are listed in Table I. An examination of the data presented in Table I shows that the solubility of Sn in the α-Cu phase is only approximately 2 wt pct, while the Sn content in the Sn-rich phase is increased to approximately 35 wt pct.

Figure 7 shows the morphology and distribution of the Sn-rich phase with and without EMS. It is found that all of the Sn-rich phases are distributed in the interdendritic region. Since in the absence of EMS the solidified structure is the well-developed dendrite, the Sn-rich phase is discontinuous and presents a fine near-spherical shape (Figures 7(a1) and (a2)). When EMS is
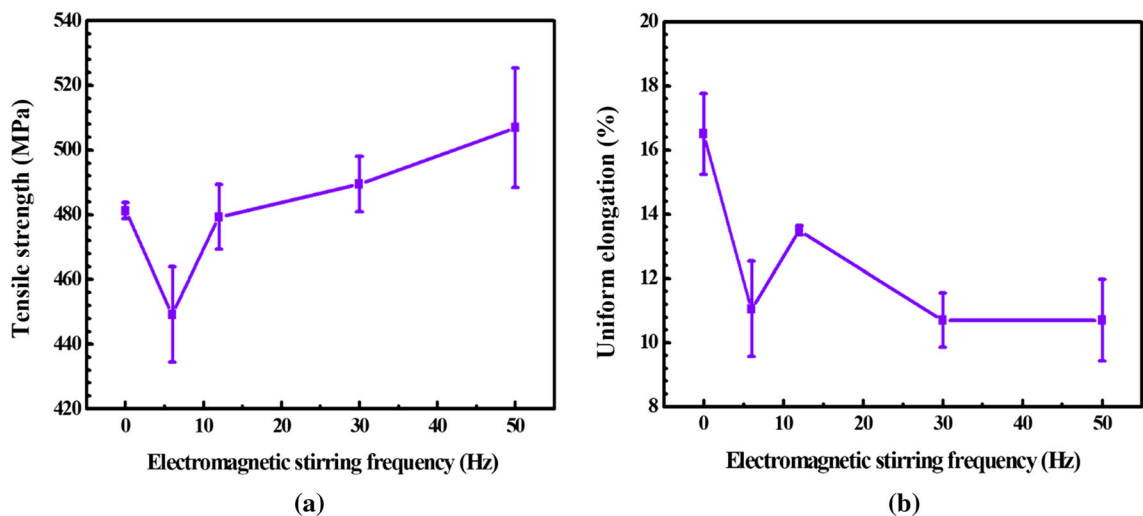

Fig. 5—Relationship between the measured tensile strength and uniform elongation as a function of the EMSF: (a) tensile strength and (b) uniform elongation.
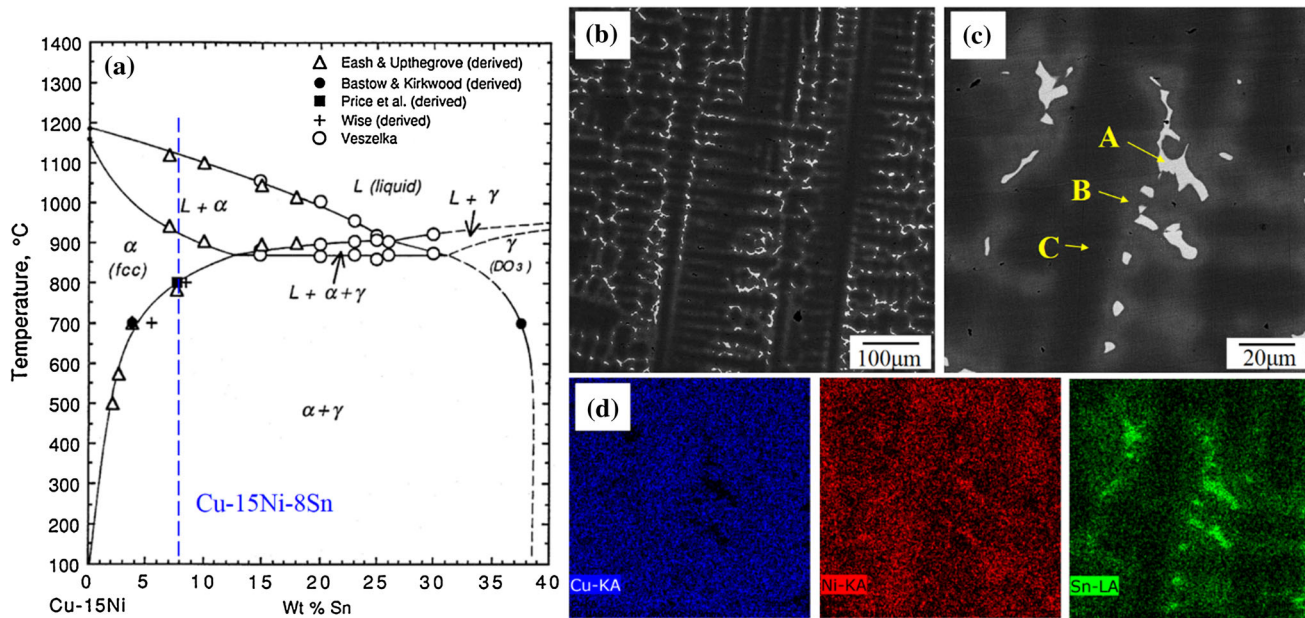
Fig. 6—Pseudo-binary phase diagram of Cu-Ni-Sn (at the isopleth of 15 wt pct Ni) and BSE images of the typical as-cast alloy phase: (*a*) pseudo-binary phase diagram, (*b*) macromorphology of alloy phases, (*c*) details of alloy phases, and (*d*) element distribution in the alloy phases.

Table I. Compositions (Weight Percent) in Different Regions Shown in Fig. 6(c)

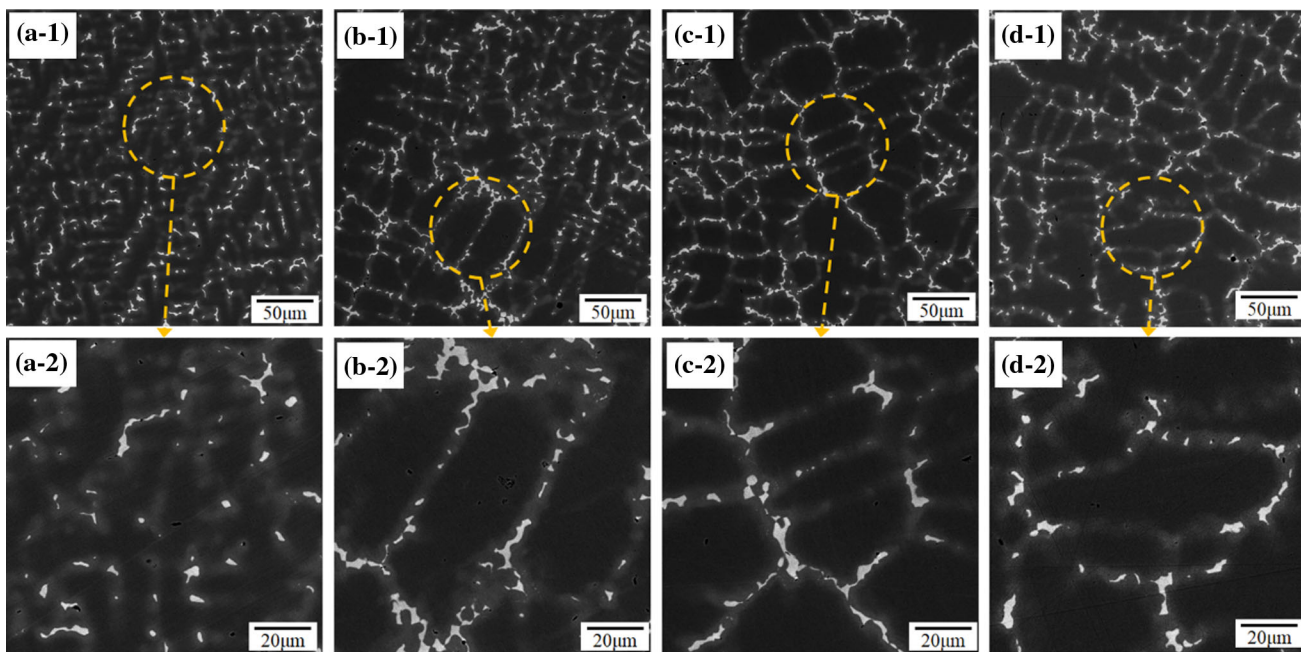| Element	A	B	C
Cu	45.60	76.96	81.07
Ni	18.48	9.85	16.15
Sn	35.91	13.19	2.78

Fig. 7—Morphology and distribution of the Sn-rich phase without and with EMS: (*a*1) and (*a*2) 0 Hz, 0 A; (*b*1) and (*b*2) 6 Hz, 120 A; (*c*1) and (*c*2) 30 Hz, 120 A; and (*d*1) and (*d*2) 50 Hz, 120 A.

applied and the solidified structure becomes undeveloped or equiaxed dendrite, the Sn-rich phase continuously distributes in the interdendritic region and presents a network-shaped distribution (Figures 7(b1) through (d2)). Moreover, the Sn-rich phase with a 6 Hz EMS becomes coarser compared to that for the samples without EMS. When EMSF increases to 30 or 50 Hz, the tendency to the network-shaped distribution is more pronounced (Figures 7(c1) through (d2)) and is associated with the presence of the rosette structure shown in Figure 4(g1).

IV. DISCUSSION

A. CET and Structure Evolution Mechanism

Figure 8 shows the effects of EMS on the CET and structure evolution mechanism ahead of the solid-liquid interface. When EMS is not applied, the temperature gradient G is so steep at the solidification front that the columnar grains will grow further into the liquid phase, as shown in Figure 8(a). When EMS is applied, the temperature field in the melt will become uniform due to the forced flow induced by EMS.[23,24] Therefore, the temperature gradient G will gradually decrease, inhibiting the further growth of columnar grains and inducing the formation of equiaxed grains ahead of the solid-liquid interface, as shown in Figure 8(b). Moreover, the dendritic fragment formed during the solidification plays an important role in the CET.[25,26] Ruvalcaba et al.[27] observed the dendritic fragmentation under normal nonforced convection conditions during the directional solidification of an Al-20 wt pct Cu alloy. They suggested that the local solute enrichment is responsible for the dendrite detachment. Liotti et al.[28] studied the effect of electromagnetic vibration on the formation of dendritic fragments by synchrotron X-ray radiography. They proposed that the electromagnetic vibration–induced interdendritic flow will lead to the enrichment of the solute at the dendrite root and then promote the production of a large number of dendritic fragments. The application of EMS will induce the electromagnetic forced flow in the mushy zone and then promote the local enrichment of solute, thereby yielding the dendritic fragment (Figure 8(b)). In addition, the high-temperature melt will be transported to the interdendritic regions by the electromagnetic-induced forced flow, also resulting in the remelting of the dendritic arms. These detached dendritic fragments will be transported into the liquid phase ahead of the solid-liquid interface and then become the core of the heterogeneous nucleus, thereby promoting the CET.

It is clear that the application of EMS will induce the CET of the solidified structure during horizontal continuous casting, but why do the grains become finer as the EMSF increases? The EMS force F can be expressed as follows[29]:

$$F \propto B_M^2(f)f \qquad [1]$$

where $B_M^2(f)$ is the magnetic induction at the considered point in the liquid alloy and f is the EMSF. The skin effect thickness δ can be expressed as[30]
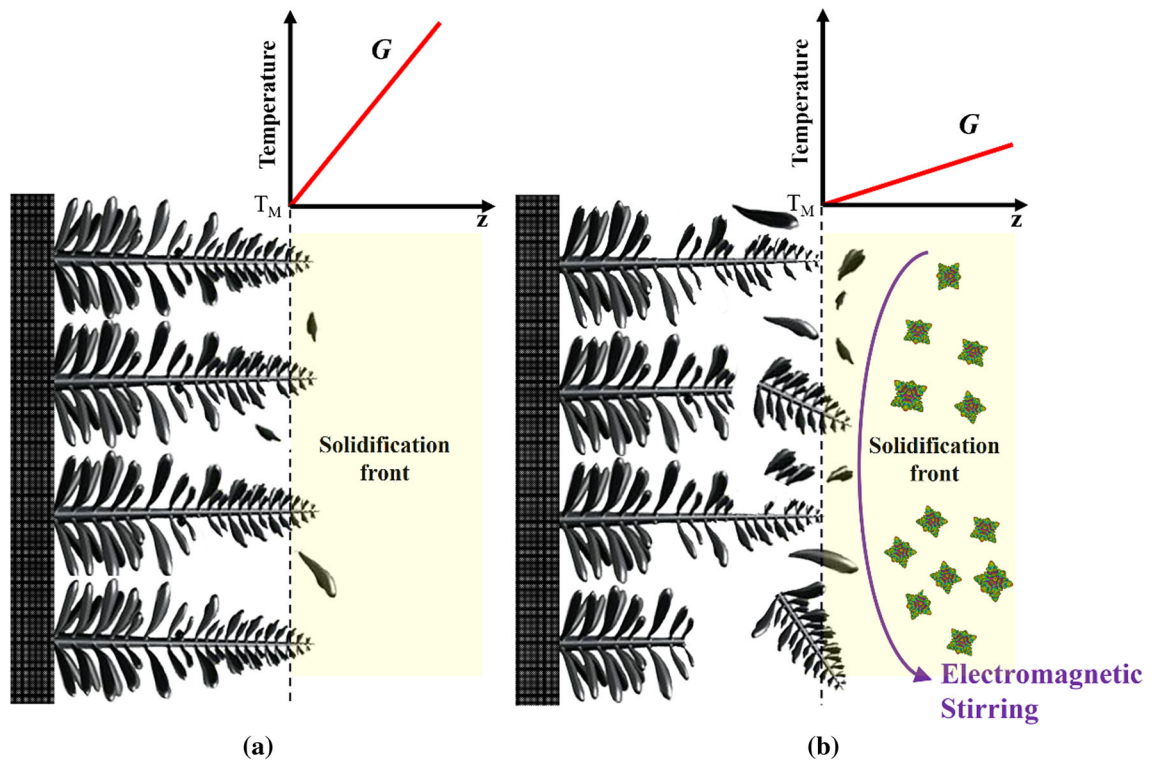

Fig. 8—Schematic diagram of the CET and structure evolution mechanism caused by EMS: (a) without EMS and (b) with EMS.

$$\delta = \sqrt{1/\pi f \mu \xi} \qquad [2]$$

where μ and ξ are the magnetic conductivity and electric conductivity of the liquid alloy, respectively. Therefore, for the same alloy, the skin effect thickness will increase with decreasing EMSF. Our experimental frequency ranges from 6 to 50 Hz and the relevant skin effect thickness ranges from 30 to 10.4 cm. When the radius of the sample is smaller than the skin effect

thickness, magnetic induction $B_M^2(f)$ may increase with the increase in the EMSF, so that the EMS force will also increase.[30] Therefore, when the EMSF increases from 6 to 50 Hz, the EMS force-driven flow in the melt will be strengthened and then the temperature gradient at the solidification front will be reduced. This not only further promotes the production of equiaxed grains but also accelerates the formation of dendritic fragments, thereby increasing the number of the nuclei in the liquid phase at the solidification front and inducing the CET.
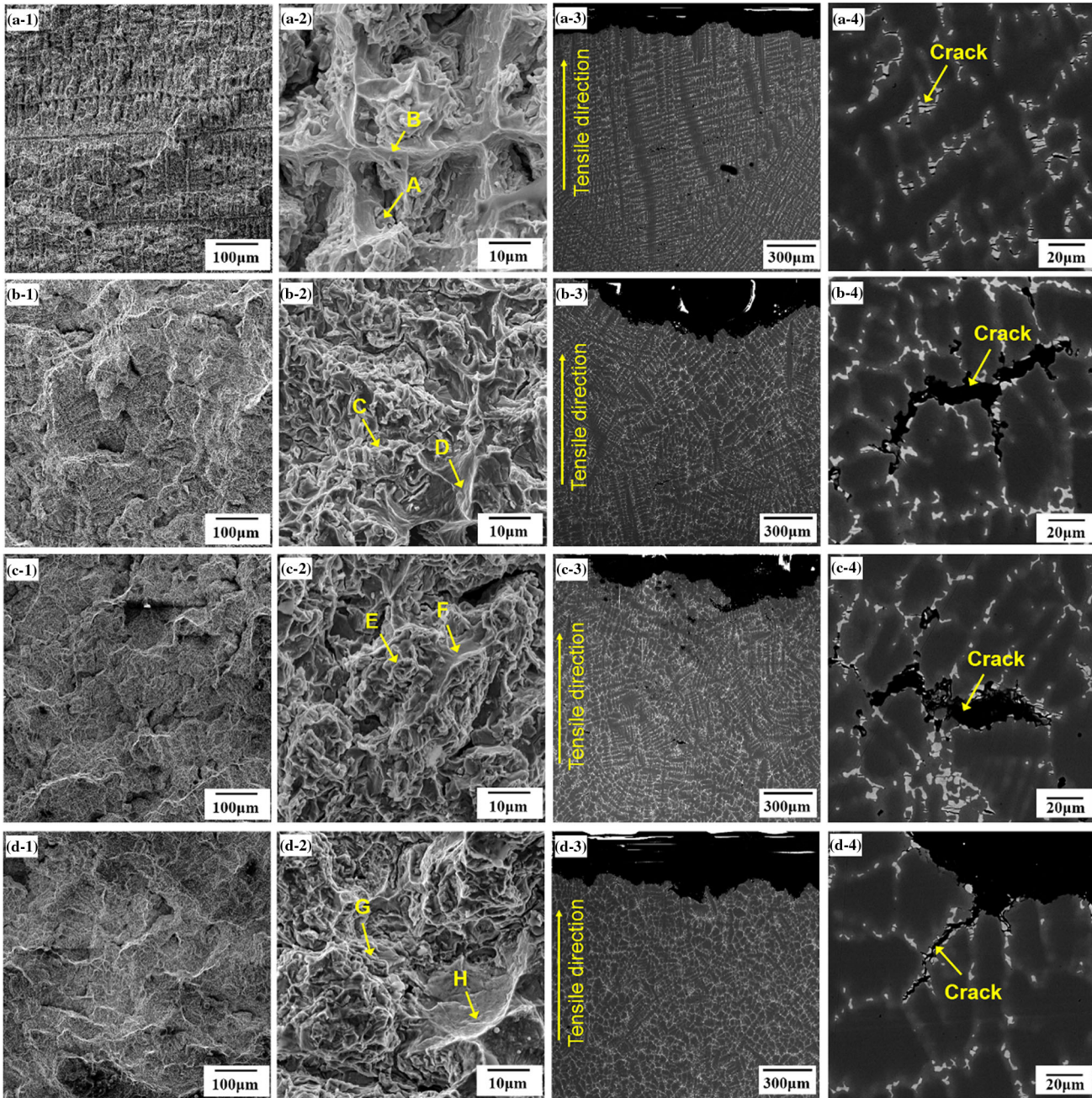

Fig. 9—Fracture surface and its longitudinal section in the samples solidified with and without EMS: (a1) and (a2) fracture surface and (a3) and (a4) corresponding longitudinal section without EMS; (b1) and (b2) fracture surface and (b3) and (b4) corresponding longitudinal section with 6 Hz EMS; (c1) and (c2) fracture surface and (c3) and (c4) corresponding longitudinal section with 30 Hz EMS; (d1) and (d2) fracture surface and (d3) and (d4) corresponding longitudinal section with 50 Hz EMS (Color figure online).

Table II. EDS Composition (Weight Percent) Analysis of the Regions Marked by Yellow Arrows in Fig. 9

Element	A	B	C	D	E	F	G	H
Cu	44.95	79.29	49.98	79.77	47.77	78.75	48.71	79.29
Ni	23.17	14.91	22.95	14.31	21.60	13.74	22.97	12.54
Sn	31.88	5.80	27.06	5.92	30.63	7.51	28.32	8.17

B. *Tensile Strength Evolution Mechanism*

To understand the evolution of tensile strength, the fracture surface and its longitudinal section in the sample solidified with and without EMS were observed by SEM, as shown in Figure 9. When EMS was not applied, the fracture surface of the tensile sample shows a combined quasi-cleavage fracture and ductile dimple fracture, but mainly quasi-cleavage fracture. The morphology of the fracture surface is dendritic like and the fracture surface is quite flat (Figure 9(a1)). The longitudinal section of the fracture surface consists of two regions (Figure 9(a2)): region A contains a large number of fine particles and region B contains many tear ridges. Table II lists the composition of these two regions. The results show that the fine particles are Sn-rich phases and the tear ridges are α-Cu solid solution phases. The BSE map of the longitudinal section shows that the cracks formed in the Sn-rich phases are extremely small (marked by the yellow arrow in Figure 9(a4)). It can be concluded that when the sample is stretched, the crack is first generated in the interdendritic region because the Sn-rich phase is brittle. Then, the crack propagates through the dendrites or secondary dendrite arms for the discontinuous distribution of the Sn-rich phase. Thus, the fracture of the Sn-rich phase is not the dominant factor during the stretching of the sample; *i.e.*, the fracture of the sample is mainly dominated by that of the α-Cu solid solution phase, thereby yielding the tear ridge and quasi-cleavage fracture.

When EMS was applied, the CET occurred in the solidified structure of the sample, inducing a change in the fracture mode. Figure 9(b) shows the fracture surface and its longitudinal section of the tensile sample solidified with a 6 Hz EMS. The fracture surface also shows a combined quasi-cleavage fracture and ductile dimple fracture, but mainly ductile dimple fracture (Figure 9(b2)). The composition of regions C and D was measured. The results show that region C is composed of the Sn-rich phases and region D is composed of the α-Cu solid solution phases. The BSE map of the longitudinal section shows that large cracks of the Sn-rich phase form during the stretching process (marked by the yellow arrow in Figure 9(b4)). When the sample is stretched, due to the continuous distribution of the Sn-rich phase in the interdendritic region, the crack will grow further along the interdendritic region instead of passing through the dendrites or secondary dendrite arms, differing from the fracture mode of the sample without EMS. This indicates that the fracture of the sample is mainly controlled by the fracture of the Sn-rich phase that results in the formation of a large number of ductile dimples. This also leads to a significant reduction in the tensile strength with EMS at 6 Hz compared to no EMS, as shown in Figure 5.

The fracture surface and its longitudinal section obtained with different EMSFs (30 and 50 Hz) are similar to those obtained at a 6 Hz EMS, as shown in Figures 9(c1) through (d4). The crack propagation is still along the continuous network Sn-rich phase. However, as the EMSF increases, the equiaxed grain size gradually decreases from 820 to 430 μm, leading to the fine-grain strengthening; *i.e.*, the tensile strength gradually increases from 449 to 506 MPa, thereby preventing the expansion of the crack along the Sn-rich phase at grain boundaries, which is consistent with the results shown in Figures 9(c4) and (d4).

V. CONCLUSIONS

In this study, the effects of EMS on micro- and macrostructure and tensile strength of horizontal continuously cast Cu-15Ni-8Sn alloys were investigated. The main conclusions are as follows.

1. The application of EMS can contribute to grain refinement, induce formation of the rosette structure, and improve tensile strength. The tensile strength was improved and reached 506 MPa due to the application of EMS (50 Hz, 120 A).
2. The forced flow induced by EMS homogenizes the temperature ahead of the solid-liquid interface, disturbing the heat flow direction from the center to the surface of the casting and promoting the CET.
3. The CET is considered to be related to the homogenization of the temperature and nucleus multiplication at the solidification front. The nucleus multiplication is mainly derived from the remelting of the dendritic arms due to the flow-induced local enrichment of the solute and heat flow.
4. The tensile strength of the Cu-15Ni-8Sn alloy was mainly controlled by the distribution of the Sn-rich phase and the grain size. When EMS is not applied, the crack propagates through the dendrites or secondary dendrite arms for the discontinuous distribution of the Sn-rich phase, thereby yielding the tear ridge and quasi-cleavage fracture. When EMS is applied, the crack propagates further along the interdendritic rosette regions, promoting crack propagation and degrading the tensile strength. With the increase in the EMSF, the grain size decreases further, improving the tensile strength.

REFERENCES

1. R.K. Ray and S.C. Narayanan: *Metall. Trans. A*, 1982, vol. 13A, pp. 565–73.
2. J.C. Zhao and M.R. Notis: *Acta Mater.*, 1998, vol. 46, pp. 4203–18.
3. J.C. Rhu and S.S. Kim: *Metall. Mater. Trans. A*, 1999, vol. 30A, pp. 2649–57.
4. B. Zhang, J. Cui, and G. Lu: *Mater. Sci. Eng. A*, 2003, vol. 355, pp. 325–30.
5. J.P. Martins, A.L.M. Carvalho, and A.F. Padilha: *J. Mater. Sci.*, 2009, vol. 44, pp. 2966–76.
6. M.T. Clavaguera-Mora, C. Comas, J.L. Touron, M. García, O. Guixà, and N. Clavaguera: *J. Mater. Sci.*, 1999, vol. 34, pp. 4347–50.
7. X. Li, Z. Guo, X. Zhao, W. Bi, F. Chen, and T. Li: *Mater. Sci. Eng. A*, 2007, vol. 460, pp. 648–51.
8. A.A. Tzavaras and H.D. Brody: *JOM*, 1984, vol. 36, pp. 31–37.
9. L. Deyong, R. Tremblay, and R. Angers: *Mater. Sci. Eng. A*, 1990, vol. 124, pp. 223–31.
10. Q. Dong, J. Zhang, B. Wang, and X. Zhao: *J. Mater. Process. Technol.*, 2016, vol. 238, pp. 81–88.
11. G. Reinhart, N. Mangelinck-Noël, H. Nguyen-Thi, T. Schenk, J. Gastaldi, B. Billia, P. Pino, J. Härtwig, and J. Baruchel: *Mater. Sci. Eng. A*, 2005, vol. 413, pp. 384–88.
12. S. Eckert, B. Willers, P.A. Nikrityuk, K. Eckert, U. Michel, and G. Zouhar: *Mater. Sci. Eng. A*, 2005, vol. 413, pp. 211–16.
13. W. Jin, F. Bai, T. Li, and G. Yin: *Mater. Lett.*, 2008, vol. 62, pp. 1585–88.
14. V. Metan, K. Eigenfeld, D. Räbiger, M. Leonhardt, and S. Eckert: *J. Alloys Compd.*, 2009, vol. 487, pp. 163–72.
15. B. Willers, S. Eckert, U. Michel, I. Haase, and G. Zouhar: *Mater. Sci. Eng. A*, 2005, vol. 402, pp. 55–65.
16. T. Campanella, C. Charbon, and M. Rappaz: *Metall. Mater. Trans. A*, 2004, vol. 35A, pp. 3201–10.
17. A. Das, S. Ji, and Z. Fan: *Acta Mater.*, 2002, vol. 50, pp. 4571–85.
18. E.O. Hall: *Proc. Phys. Soc.*, 1951, vol. 64, pp. 747–53.
19. N.J. Petch: *J. Iron Steel Inst.*, 1953, vol. 174, pp. 25–28.
20. H. Kato: *Mater. Sci. Eng. A*, 2015, vol. 639, pp. 540–49.
21. M. Li, T. Tamura, N. Omura, and K. Miwa: *J. Alloys Compd.*, 2010, vol. 494, pp. 116–22.
22. H. Zhang, Y.Z. He, X.M. Yuan, and P. Ye: *Appl. Surf. Sci.*, 2010, vol. 256, pp. 5837–42.
23. J.D. Hunt: *Mater. Sci. Eng.*, 1984, vol. 65, pp. 75–83.
24. A. Hellawell, S. Liu, and S.Z. Lu: *JOM*, 1997, vol. 49, pp. 18–20.
25. R.H. Mathiesen, L. Arnberg, P. Bleuet, and A. Somogyi: *Metall. Mater. Trans. A*, 2006, vol. 37A, pp. 2515–24.
26. X. Li, A. Gagnoud, Y. Fautrelle, Z.M. Ren, R. Moreau, Y.D. Zhang, and C. Esling: *Acta Mater.*, 2012, vol. 60, pp. 3321–32.
27. D. Ruvalcaba, R.H. Mathiesen, D.G. Eskin, L. Arnberg, and L. Katgerman: *Acta Mater.*, 2007, vol. 55, pp. 4287–92.
28. E. Liotti, A. Lui, R. Vincent, S. Kumar, Z. Guo, T. Connolley, I.P. Dolbnya, M. Hart, L. Arnberg, and R.H. Mathiesen: *Acta Mater.*, 2014, vol. 70, pp. 228–39.
29. P.P. Sahoo, A. Kumar, J. Halder, and M. Raj: *ISIJ Int.*, 2009, vol. 49, pp. 521–28.
30. H.K. Moffatt: *Phys. Fluids*, 1991, vol. 3, pp. 1336–43.